fluids

MDPI

Article

On the Convergence, Node Collocation, and the Disc-Edge Singularity of a Vortex-Ring/Vortex-Cylinder Free-Wake Model for the Uniformly Loaded Actuator Disc

Alois Peter Schaffarczyk

Faculty of Mechanical Engineering, Kiel University of Applied Sciences, Grenzstrasse 3, D-24149 Kiel, Germany; alois.schaffarczyk@haw-kiel.de

Abstract

Free-wake vortex-ring models are the simplest way of describing a uniformly loaded actuator disc consistently with the Euler equations, i.e., including the radial velocity that accompanies slipstream contraction or expansion. This paper examines the numerical behavior of this model class using an independent open-source FORTRAN 90/95 implementation and a 1:1 Python (v3.12) replica, for the propeller case ($c_T = 1$) and the Betz case ($c_T = -8/9$). Three results are reported. First, the two convergence measures in common use—the residual of the wake (sheet) equations and the deviation of the power coefficient c_P from momentum theory—are shown not to be equivalent: the latter has a discretization floor and is not monotone, so it is unsuitable as a stopping criterion, and accuracy figures obtained with it are sometimes misleading. Second, the discrete Kelvin–Helmholtz saw-tooth mode is stabilized by a damping factor proportional to $\sqrt{z}$, which reaches the residual floor within a few hundred instead of 10^4 iterations; the remaining c_P fluctuation band reflects the unresolved disc-edge region and is removed by node collocation with a spacing-proportional vortex kernel, which converges to a unique fixed point with machine-level residuals and $c_P - (-16/27) = +4.7 \times 10^{-5}$. Third, the converged solutions show a bounded edge strength with fitted exponent $a = 0.00 \pm 0.04$ in $\gamma \propto s^a$, differing from both the $s^{-1/2}$ spiral and the constant-γ proposals in the literature; it is explained why single-valued, regularized sheet discretizations cannot decide this question.

Keywords: actuator disc; vortex ring model; free wake; potential flow; momentum theory; Betz limit; slipstream; edge singularity; convergence; Richardson extrapolation; wind turbine aerodynamics

Check for updates

Academic Editor: Rodolfo Bontempo

Received: 30 July 2026
Revised: 9 September 2026
Accepted: 11 September 2026
Published: 14 September 2026

Copyright: © 2026 by the author. Licensee MDPI, Basel, Switzerland. This article is an open access article distributed under the terms and conditions of the Creative Commons Attribution (CC BY) license.

1. Introduction

Rotors, and wind-turbine rotors in particular, have been modeled by an axisymmetric actuator disc (AD) for more than 150 years [1,2]. In its classical form, the model is evaluated by an integral momentum balance in which only the axial velocity component appears [3]. It is easily shown, however, that such a description is not consistent with the differential equations of inviscid flow, Euler's equations,

$$\nabla \cdot \mathbf{u} = 0, \tag{1}$$

$$\rho \frac{D\mathbf{u}}{Dt} = -\nabla p + \mathbf{f}, \tag{2}$$

because the radial velocity component that necessarily accompanies a contracting or expanding slipstream is discarded. Among the ways of restoring consistency without solving (1) and (2) numerically, vortex-ring (free-wake) methods [4,5] are arguably the simplest: the wake boundary is represented by a free vortex sheet whose position and strength are obtained from two physical conditions, and the velocity field follows from the Biot–Savart law in closed (elliptic-integral) form.

Vortex-wake modeling of rotors is, of course, a mature field, and the model studied here is its simplest member rather than a new idea. Free-wake methods built from vortex-line (filament) elements were developed for helicopter rotors from the 1970s onwards and are documented comprehensively by Johnson [6] and Leishman [7]; their numerical properties—stability, consistency, and convergence of the time-marching free-wake iteration—were analyzed by Bhagwat and Leishman [8], a study whose questions are close to those of the present paper. Vortex-particle methods [9] represent the wake by Lagrangian vorticity carriers instead of connected elements. Miller [10] showed that for the hovering rotor, the helical wake can be replaced, to leading order, by a system of vortex rings, which is precisely the approximation on which the axisymmetric actuator-disc wake models discussed below rest. The present work should therefore be read as a re-examination, with present-day numerical means, of the axisymmetric vortex-ring limit of these classical methods, and its results on convergence measures, damping, and collocation are intended to be transferable to the more general filament methods.

Starting from Øye's 1990 paper [11], this approach was developed further and applied by van Kuik and Lignarolo [12] and by Bontempo and Manna [13,14]; Conway [15] generalized the underlying analytical framework to non-uniform heavy loading. Despite this long history, three questions of practical relevance for anybody implementing such a model have, to the best of the author's knowledge, not been answered in the open literature:

1. What do the usual convergence measures actually measure? Free-wake AD codes are commonly stopped either on a residual of the wake (sheet) equations or on the deviation of the computed power coefficient c_P from its momentum-theory value. Are these two criteria equivalent, and does either of them certify a converged solution?
2. Is the free-wake fixed-point iteration stable, and at what price? A cylindrical vortex sheet is Kelvin–Helmholtz (KH) unstable, so any explicit update of the sheet position must be damped. Which damping keeps the scheme stable without corrupting the solution near the disc edge?
3. What does a converged free-wake solution say about the disc-edge singularity? Two mutually exclusive edge behaviors have been proposed in the literature: a self-similar (Prandtl/Kaden) spiral with $\gamma \propto s^{-1/2}$ [5,16] and a bounded sheet strength with logarithmic velocity singularities [17].

The present paper answers these questions with the help of an independent, open-source FORTRAN 90/95 [18] implementation of the vortex-ring/vortex-cylinder model for a uniformly (constantly) loaded actuator disc, together with a 1:1 Python (v3.12, with `numpy` and `scipy`) replica of the same algorithm that allows systematic parameter studies. The main findings are:

- The sheet residual and the momentum-theory deviation are *not* equivalent (Section 3). The latter possesses a discretization floor and is not even monotone during the iteration; using it as a stopping criterion can flatter the apparent accuracy by more than an order of magnitude.
- The KH saw-tooth mode is controlled by a damping factor $\lambda \propto \sqrt{z}$, which is stable for all ring numbers tested and equilibrates the edge region about two orders of magnitude faster than the $\lambda \propto z$ damping used previously (Section 3.2).

- With midpoint collocation, c_P retains a small residual fluctuation band that shrinks with the discretization but not with the number of iterations; it is a property of the unresolved edge region, not an iteration deficiency (Section 3.3). Replacing midpoint collocation by node collocation with a spacing-proportional vortex kernel (Section 2.4) removes the band entirely and yields a unique fixed point with machine-level residuals.
- The converged solutions of this model class show a *bounded* edge strength, with a fitted exponent $a = 0.00 \pm 0.04$ in $\gamma \propto s^a$—different from both proposals cited above. It is shown why a single-valued, midpoint-, or kernel-regularized sheet discretization is structurally unable to represent a rolled-up spiral, and why this does not affect the computed c_P (Section 5).

The code, its Python replica, the configuration files of all cases discussed here, and the GNUPLOT/Python post-processing scripts are available at https://github.com/Schaffarczyk/RingsCylinderActuatorDisk/ (accessed on 10 September 2026).

2. Model and Numerical Method

2.1. Model Description

Axisymmetric coordinates (z, r) are used with the velocity $\mathbf{u} = (u_z, u_r)$, non-dimensionalized with the undisturbed wind speed, $u_z(r)_{z\to-\infty} = 1$, and with the disc radius, so that the disc occupies $z = 0$, $0 \le r < 1$. Its edge $\mathbf{r}_E = (0, 1)$ may carry a singularity, i.e., a point at which $\mathbf{u}$ is not defined; this is the subject of Section 5.

The wake boundary is modeled by a piecewise linear vortex sheet which starts at $\mathbf{r}_{edge} = (0, 1)$ and ends at $\mathbf{r}_{Cyl} = (z_{SIVC}, r_{SIVC})$, where a semi-infinite vortex cylinder (SIVC) with tangential vorticity is appended. For $0 < z < z_{SIVC}$, N vortex rings of strength γ are placed with non-uniform (cosine-clustered) spacing at positions (zsl_i, rsl_i),

$$z_i = z_{SIVC}(1 - \cos\varphi_i), \tag{3}$$

$$\varphi_i = \frac{\pi}{2} \cdot \frac{i}{N}, \qquad 1 \le i \le N, \tag{4}$$

so that the resolution is highest at the disc edge, where the solution varies most rapidly. This part of the approach is identical to that of [13,14].

The single physical parameter of the model is the thrust coefficient c_T, with $c_T > 0$ for the propeller case (induced velocities > 0) and $c_T < 0$ for the turbine case; momentum theory is valid for $-1 \le c_T < \infty$. Several exact relations follow from momentum theory and are used below both as initial conditions and as reference values. The asymptotic radial extension of the slipstream is

$$r^{sl}_{z\to\infty} \equiv r_{SIVC} = \sqrt{\frac{1 + \sqrt{1 + c_T}}{2\sqrt{1 + c_T}}}, \tag{5}$$

giving $r_\infty = 0.9239$ for $c_T = 1$ and $r_\infty = \sqrt{2} = 1.4142$ for $c_T = -8/9$ (the Betz case). The value of the total (i.e., inflow included) stream function on the slipstream far downstream is

$$\psi_{wake} = \frac{1}{4}\left(1 + \sqrt{1 + c_T}\right), \tag{6}$$

i.e., $\psi_{wake} = 0.603553$ for $c_T = 1$ and $\psi_{wake} = 1/3$ for $c_T = -8/9$. (If only the induced part of the stream function is used, the corresponding value is $c_T/(4\sqrt{1 + c_T})$; the code works with the total stream function, Equation (6)). The model parameters are summarized in Table 1.

Table 1. Major and minor parameters of the model. The names are those of the configuration file `inpa.dat` of the code.

Name	Meaning
major	
c_T	thrust coefficient
restart	LOGICAL; if `.true.` the code restarts from an existing `sls.DAT`
N	number of vortex rings
ZSIVC	axial location of the semi-infinite vortex cylinder
minor	
selfind	(0, 1), self-induction off/on
update	(0, 1), default = 1, debugging only
maxiter	maximum number of slipstream iterations ($\leq$2000 used)
under	under-relaxation parameter, see Section 2.3
epsSL	stop tolerance for the sheet residual errsl
wakety	initial wake shape: 1 = exponential, Equation (9); 2 = fit of the data of [19]; 3 = algebraic, Equation (10)
wake-a	decay parameter a for wakety = 1
iter-sc	update scheme: 3 = ψ-condition; 7 = ψ with $\sqrt{z}$-damping; 8 = 7 + Anderson acceleration; V4 = node collocation, Section 2.4

2.2. Induced Velocities

An accurate evaluation of the induced axial and radial velocities is the key to any arbitrarily accurate—that is, successful—implementation. The computation is split into three parts:

1. the velocities induced by the $N-1$ remaining vortex rings on the ring under consideration, $0 \leq z \leq z_{SIVC}$;
2. the self-induced velocity of the ring under consideration. Bontempo's expressions [14] (Equations (6) and (7) therein) are used, which, remarkably, do not contain any core parameter:

$$v_{z,m\to m} = \gamma_m \left\{ -\frac{\beta_{m+1}-\beta_m}{8\pi}\cos\beta_m - \frac{ds_m}{4\pi r_m}\left[\log\left(\frac{8\pi r_m}{ds_m}\right) - 0.25\right]\right\}, \tag{7}$$

$$v_{r,m\to m} = \gamma_m \left\{ \sin\beta_m - \frac{\beta_{m+1}-\beta_m}{8\pi}\right\}, \tag{8}$$

   with β_m the local slope of the sheet at ring m, r_m its radial position, and ds_m the distance between the two neighboring rings. For the self-induction of vortex rings in general see, e.g., [20];
3. the velocities induced by the semi-infinite vortex cylinder at z_{SIVC}, for which the closed-form expressions of [4] (chapter 36) are used.

To avoid singular velocities on the sheet itself, all velocities are evaluated at the arithmetic midpoints of two neighboring (singularity-carrying) sheet points. No artificial vortex core is introduced. This *midpoint collocation* is the classical choice; Section 2.4 discusses a structurally different alternative.

As an independent check against implementation errors, three different sets of equations for the induced velocities can be selected at run time: (i) Equations (1)–(7) of [13,14], (ii) Equation (D1) of [5], and (iii) the expressions of chapters 33 and 36 of [4]. All three agree to the accuracy of the elliptic-integral evaluation. For consistency of nomenclature, the formulation of Branlard [4] is used throughout. The complete and incomplete elliptic integrals (chapter C.4 of [4]) are evaluated with the open-source routine RFLof Carlson and Notis [21];

the implementation was verified against MATHEMATICA (Wolfram Research, Champaign, IL, USA) to 10 significant digits.

The accuracy of the induced velocities was verified separately for the ring part ($0 < z < z_{SIVC}$) and for the cylinder part ($z \geq z_{SIVC}$), and against the data of van Kuik [19].

2.3. Free-Wake (Slipstream) Iteration

The shape of the slipstream is determined by the induced velocities and vice versa, through two conditions [5,13,14]:

- the sheet must be force free, implemented as $\gamma = -c_T/(2u_s)$ with $u_s^2 = (1+u_z)^2 + u_r^2$;
- the sheet must be aligned with the flow, implemented as $\psi_w(z) = \psi_w(\infty) = \psi_{wake}$, Equation (6).

An initial guess for the slipstream shape reduces the number of iterations. Three options are implemented: a cylinder of radius r_{SIVC}; the prescribed exponential shape

$$r_{sl}(z) = r_{SIVC} + (r_0 - r_{SIVC}) \exp(-a\, z); \tag{9}$$

and a prescribed algebraic shape deduced from the axial velocity on the axis of a vortex cylinder, attributed by van Kuik [5] to Snel and Schepers,

$$u_z(r=0,z) = \frac{\gamma_\infty}{2}\left(1 + \frac{z}{\sqrt{z^2 + r_{SIVC}^2}}\right). \tag{10}$$

In Equation (9), r_{SIVC} is given by Equation (5) while the decay parameter a (not to be confused with the axial induction factor) has to be estimated, $a \approx 1 \ldots 2$. Figure 1 shows a two-parameter fit of the $c_T = 1$ slipstream data of van Kuik [19], who normalizes with $r_{SIVC,vK} := 1$; the fit gives $r_0 = 1.03498$, $r_{SIVC} = 1.00006$ (as it should), and $a = 1.01452$.

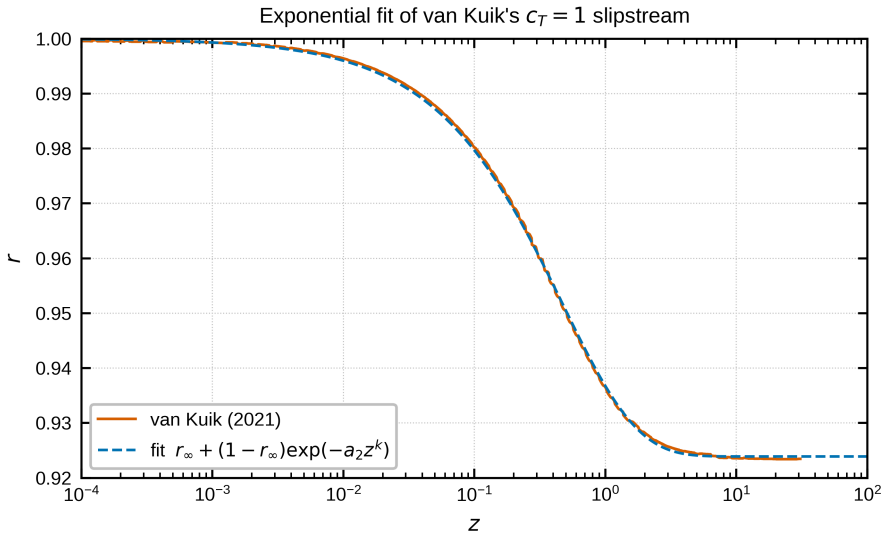


Figure 1. Two-parameter (a_2, k) fit of the $c_T = 1$ slipstream of van Kuik [19] according to $r(z) = r_\infty + (1 - r_\infty)\exp(-a_2 z^k)$ with $a_2 = 1.7743$ and $k = 0.7570$. Abscissa: axial coordinate z (logarithmic); ordinate: slipstream radius r.

Several update schemes for the sheet position have been implemented, selected by the parameter `iter-sc` (the numbers below are the values of this parameter, cf. Table 1; the intermediate values 4–6 belong to discarded experimental variants):

(1) Equations (13) and (14) of [14];

(2) shifting the sheet points normal to the current sheet direction;
(3) van Kuik's [5] Equation (D.12),

$$\partial r(z) = \frac{\partial \psi}{r\, u_z}, \qquad \partial \psi = \psi(\text{sheet}, z) - \psi_{wake}, \tag{11}$$

damped with $\lambda(z) = \min(z, 0.1) \cdot \mathit{under}$;
(7) as (3), but with the damping factor $\lambda(z) = \min\!\left(0.1,\ \mathit{under} \cdot \sqrt{z}\right)$;
(8) as (7), plus Anderson acceleration (window 4) of the resulting fixed-point iteration.

Schemes 7 and 8 are the recommended ones; among the older schemes, No. 3 was preferred. All schemes may be under-relaxed, with $\mathit{under} = 0.001 \ldots 0.01$ for scheme 1, <0.01 for scheme 2, $0.1 \ldots 0.9$ for scheme 3, and $0.05 \ldots 0.1$ for schemes 7 and 8, where *under* acts as the prefactor of $\sqrt{z}$.

The iteration is terminated when (i) the number of iterations exceeds `maxiter`, (ii) the sheet residual satisfies errsl $\leq$ `epsSL`, or (iii) (schemes 7 and 8) c_P has stopped moving, $|\Delta c_P| < 10^{-6}$ over the last 100 iterations (Cauchy criterion). In earlier versions of the code, the iteration was stopped when err$c_P := |c_P - c_{P,mom}|$ fell below a prescribed tolerance. As shown in Section 3, errc_P is *not* a valid iteration criterion.

2.4. Node Collocation with a Spacing-Proportional Vortex Kernel

The analysis of Sections 3 and 5 identifies a structural conflict of the midpoint-collocation scheme: stability requires a position-dependent damping, the edge region remains under-determined, and c_P retains a fluctuation band. A fourth version of the code therefore changes the discretization itself, following van Kuik and Lignarolo [12] (Appendices A and B therein):

1. N vortex rings with circulations Γ_i are collocated *at the nodes* (z_i, r_i); ring 1 is pinned at the disc edge $(0, 1)$ and exempted from the boundary conditions, in line with the discussion of the leading edge in [12] (Section 4.3 therein).
2. A *vortex kernel* regularizes all evaluations at distances $\rho < \frac{1}{2}\beta\, ds_i$ using smoothed (Marshall-type) expressions. Deviating from the fixed $\delta = 0.002$ of [12], the kernel radius is taken proportional to the local spacing, $\delta_i = \beta\, ds_i$ with $\beta = e^{-1/2} \approx 0.607$, which matches the analytic contribution of the local sheet strip. A fixed δ biases c_P by $\sim 10^{-2}$ as soon as $ds \gg \delta$, i.e., as soon as the spacing varies appreciably along the sheet, as it does with the clustering of Equations (3) and (4).
3. The update is single-phase with *uniform* damping $d = 0.05$,

$$\Gamma_i \leftarrow \Gamma_i + d(\Gamma_i^* - \Gamma_i), \quad \Gamma_i^* = -\frac{c_T}{2 v_i}\, ds_i, \qquad r_i \leftarrow r_i + d\, \frac{\psi_{wake} - \psi_i}{r_i (1 + v_{z,i})}. \tag{12}$$

The kernel removes the saw-tooth mode (Section 3.2), so no z-dependent damping is needed. The normal-velocity ("fine-tuning") phase of [12] (Appendix B.3 therein) was tested and found to be neither stable nor necessary in this implementation: after the ψ-phase, $v_n \approx 3 \times 10^{-2}$ at the edge and $\approx 2 \times 10^{-3}$ on the sheet; it is retained only as a diagnostic (see Section 5.4).

2.5. Implementation Notes

The code is written in FORTRAN 90/95 [18] and deliberately kept simple: a minimal set of language features is used and no algorithmic "tricks" are applied, so that the source remains readable and maintainable. It consists of three files only: `mem.f` (global variables), `VortexCode.f` (the slipstream iteration loop) and `SubA.f` (the function library, including the elliptic integrals). Compilation uses GNU Fortran [22] with the mandatory options

`-fno-automatic` (local variables in subroutines and functions) and `-fdefault-real-8` (64-bit reals, ≈15–16 decimal digits). The latter must be applied to *all* source files including `mem.f`; otherwise the global arrays of the module remain 32-bit while the rest of the code works in double precision—an error that is easily overlooked and that limits the attainable residual to $\sim 10^{-6}$.

The power coefficient is obtained from the axial velocity at the disc following Equations (15)–(20) of [14]. The radial integration of $u_z(z = 0, r)$ from $r = 0$ to $r = 1$ uses Simpson's rule; since this is second-order accurate, at least 10^3 points are required for an accuracy of 10^{-6}, and 3000 points are used throughout. As expected for a scheme in which every ring interacts with every other ring, the CPU time scales as $\sim N^2$ (Figure 2).

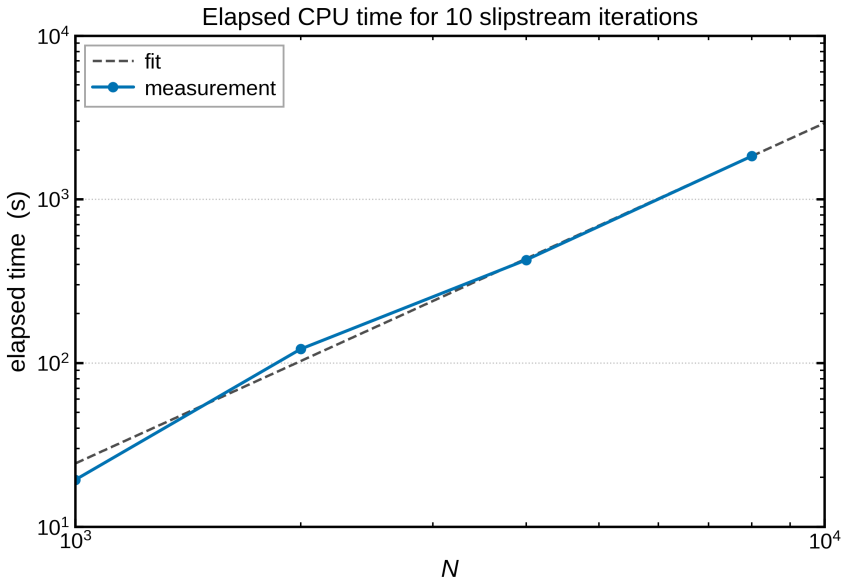


Figure 2. Elapsed CPU time for 10 slipstream iterations as a function of the number of rings N (double logarithmic; symbols: measurement, line: fit). Hardware: Intel i3-4160 at 3.6 GHz; operating system: openSUSE Leap 42.3 Linux, kernel 4.12.14-lp151.28.44-default.

All results reported below were, in addition, reproduced with a 1:1 Python replica of the code (`numpy/scipy`, identical Carlson elliptic integrals), which made the systematic parameter studies of Section 3 ($N = 300 \ldots 4000$, up to 15,000 iterations) practicable.

3. Convergence Measures, Stability, and the Power Coefficient

A numerical scheme deserves to be called meaningful only if it satisfies the elementary requirement

$$\forall\, \epsilon > 0 \;\; \exists\, n \in \mathbb{N} : \;\text{after } n \text{ iterations the result is accurate to } \epsilon. \tag{13}$$

Whether a given free-wake code satisfies Equation (13) depends on which quantity "the result" refers to. This section shows that the two quantities commonly monitored behave very differently in this respect.

3.1. What the Two Convergence Measures Measure

The code monitors

$$\mathrm{errsl} = \frac{1}{N} \sum_{i=1}^{N} |\psi(z_i, r_i) - \psi_{wake}| ds_i, \tag{14}$$

$$\mathrm{err}c_P = \left| \frac{c_P - c_{P,mom}}{c_{P,mom}} \right|. \tag{15}$$

These measure two fundamentally different things. errsl is the residual of the *discrete* system: it can, in principle, be driven to zero by iteration alone. errc_P is the distance between the discrete solution and the *continuum* momentum-theory limit. Even at the exact discrete fixed point (errsl $= 0$), errc_P retains a discretization floor made up of (i) a contribution $\sim 1/N^2$ from the ring discretization (Table 2), (ii) a truncation error from the finite z_{SIVC}, and (iii) the contribution of the disc-edge region, which the panels cannot resolve (Section 5). Consequently, errsl $< 10^{-8}$ neither implies nor can imply err$c_P < 10^{-8}$.

Table 2. Error in c_P as a function of the number of rings, obtained with the midpoint scheme and the iteration stopped at err$c_P < 10^{-6}$ ($z_{SIVC} = 200$). See Section 3.1 for a detailed discussion.

Number of Rings N	Error in c_P
4000	1.5×10^{-4}
8000	1.7×10^{-5}
16,000	1.6×10^{-6}

Three further mechanisms decouple the two measures:

1. **The *ds*-weighting makes** errsl **blind at the disc edge.** With the cosine clustering of Equations (3) and (4), $ds \approx z_{SIVC}\pi^2/(4N^2)$ at the first ring—precisely where $|\Delta\psi|$ is largest (edge singularity) and where c_P is most sensitive, because the weight $2r\,dr$ of the power integration concentrates near $r = 1$. The code therefore also reports the unweighted max $|\Delta\psi|$.
2. **A damping factor $\lambda \propto z$ freezes the edge.** The relaxation factor $\lambda(z) = \min(z, 0.1)$ of scheme 3 vanishes at the disc, so the equilibration time of the first ring is $\sim 1/z_1 \approx 10^4$ iterations for $N = 600$, $z_{SIVC} = 25$: errsl reaches its floor after ≈200 iterations while c_P keeps creeping for thousands of iterations. A reference run over 15,000 iterations never reached a fixed point; c_P wandered by $\pm 2 \times 10^{-3}$ around $c_{P,mom}$ at errsl $\approx 10^{-9}$.
3. errc_P **is not monotone.** During this creep c_P *crosses* $c_{P,mom}$. Values as small as err$c_P \sim 10^{-6}$ occur at these zero crossings without indicating convergence at all.

Item 3 has a direct practical consequence: accuracy tables obtained by stopping the iteration on errc_P—such as Table 2, which is representative of what is found in the literature—must be read with care, since they may report the position of a zero crossing rather than a converged result.

Two implementation errors were found and corrected in the course of this analysis and are reported here because they are easy to reproduce in any comparable code: the segment length *ds* entering Equation (14) was taken from a stale variable, which made errsl about 50 times too large, and the under-relaxation factor was applied twice, giving an effective relaxation $\min(z, 0.1) \cdot under^2$.

3.2. Stability: The Saw-Tooth (Kelvin–Helmholtz) Mode

A cylindrical vortex sheet is KH unstable; the discrete manifestation is a saw-tooth mode on the grid scale. Systematic tests with the Python replica ($N = 600$) gave the following picture:

- undamped Newton steps, Equation (11) with $\lambda = 1$: the saw-tooth amplitude grows from 10^{-2} to $O(1)$ and c_P diverges;
- constant damping: marginally stable at $\lambda \approx 0.003$ for $N = 600$ and unstable for larger λ; the threshold *decreases* with N;
- $\lambda \propto z$ (scheme 3): stable, but the edge is frozen (see Section 3.1);
- $\lambda = \min(0.1, under\sqrt{z})$ (scheme 7): stable for $N = 600$ *and* $N = 1200$, with an edge equilibration about 100 times faster than scheme 3.

Purely local alternatives—per-station Newton iterations with a geometry-consistent finite-difference Jacobian, Gauss–Seidel sweeps, and naive streamline tracing—were also tested. They either diverge or converge to a shifted fixed point: the ring-to-ring coupling near the edge is too strong for any purely local update. This is a genuine property of the problem, not of a particular implementation, and explains why free-wake AD codes need global (or strongly damped) updates.

It should be stated clearly what the damping does and does not mean physically. The saw-tooth mode is the discrete counterpart of a real instability: a cylindrical vortex sheet is Kelvin–Helmholtz unstable, a system of vortex rings is unstable to pairing and leap-frogging, and helical tip vortices are unstable to the mutual-inductance modes analyzed by Widnall [23] and, for rotor wakes, by Sørensen [24]. Real wakes accordingly exhibit vortex jitter, roll-up of the sheet into discrete clumps and, a few radii downstream, breakdown of the coherent structure, as seen for instance in the near-wake measurements of Lignarolo et al. [25]. The converged solution sought here is therefore not a state that a real wake ever attains; it is the fixed point of the *steady, axisymmetric* model equations, i.e., the inviscid mean-flow idealization on which momentum theory and the actuator-disc concept rest. Damping is the numerical device that selects this fixed point by suppressing the unstable modes, and the convergence certified in the following sections is convergence of the discrete equations to that fixed point, not a statement about the stability of the flow. The idealization is justified in the same sense as momentum theory itself: the first few radii of the wake, which determine the disc loading and c_P, are only weakly affected by the instability, whereas the far wake is represented by its time-averaged (cylindrical) equivalent. The time-marching filament methods of [7,8] face the same issue in a different guise, in that the physical instability and numerical instability of the wake have to be separated there as well.

3.3. The c_P Band and Its Reduction by Richardson Extrapolation

With scheme 7, errc_P drops to $\approx 10^{-4}$ within $\approx$350 iterations ($N = 600$, $z_{SIVC} = 25$) and then oscillates slowly around $c_{P,mom}$; with the Anderson-accelerated scheme 8, errsl reaches its floor three to four times faster still. The remaining oscillation band of c_P, $\pm(3 \ldots 5) \times 10^{-4}$ for $N = 600$, $z_{SIVC} = 25$, is *not* an iteration deficiency: at errsl $\approx 10^{-8}$ the discrete equations leave the unresolved edge region—and with it c_P—undetermined within this band. Different (all stable) update schemes converge to slightly different pseudo-solutions inside the same band. The band shrinks with increasing N and z_{SIVC}, but not with more iterations.

The code therefore reports, in addition to the last iterate, an exponentially weighted moving average of c_P (time constant $\approx$ 50 iterations) and the fluctuation band $\pm(\max - \min)/2$ over the last 100 iterations. It is recommended to quote c_P as "average $\pm$ band" and reducing the band by an N-study with Richardson extrapolation.

Table 3 and Figure 3 show such a study for the Betz case ($c_T = -8/9$, exact momentum-theory value $c_{P,mom} = -16/27 = -0.592593$) computed with scheme 7 at $z_{SIVC} = 50$ and 1100–1200 iterations per run. All extrapolation variants land at $c_{P,\infty} = -0.59250 \cdots - 0.59253$, i.e., within $(0.6 \ldots 1.1) \times 10^{-4}$ of $-16/27$. The observed convergence order is $p \approx 1.2$—edge-dominated, and clearly not the smooth $1/N^2$ of the ring discretization away from the edge. The recommended citation for this protocol is $c_P = -0.59251 \pm 0.00007$.

A complementary study at fixed $N = 2000$ with $z_{SIVC} = 50$, 100, and 200 gave the perhaps counter-intuitive result that a *larger* z_{SIVC} degrades the result: the bands grow from 6.8×10^{-5} to 2.0×10^{-4} and 3.9×10^{-4}, and the means move away from $-16/27$. The reason is that at fixed N, all cell sizes scale $\propto z_{SIVC}$—the first (edge) cell even $\propto z_{SIVC}/N^2$—so the

loss of resolution outweighs the smaller truncation error of the cylinder, which is already subdominant at $z_{SIVC} = 50$. The practical rule is therefore: use $z_{SIVC} = 50$ and invest the available effort in N; a double extrapolation in (N, z_{SIVC}) is unnecessary.

Table 3. N-study for the Betz case, $z_{SIVC} = 50$, midpoint collocation with scheme 7. $\bar{c}_P$ is the exponentially weighted moving average, the band is $\pm(\max - \min)/2$ over the last 100 iterations.

N	$\bar{c}_P$	Band$\pm$	$\bar{c}_P - c_{P,mom}$
1000	-0.5923884	3.8×10^{-4}	$+2.0 \times 10^{-4}$
2000	-0.5924765	6.8×10^{-5}	$+1.2 \times 10^{-4}$
4000	-0.5925145	5.3×10^{-5}	$+7.8 \times 10^{-5}$

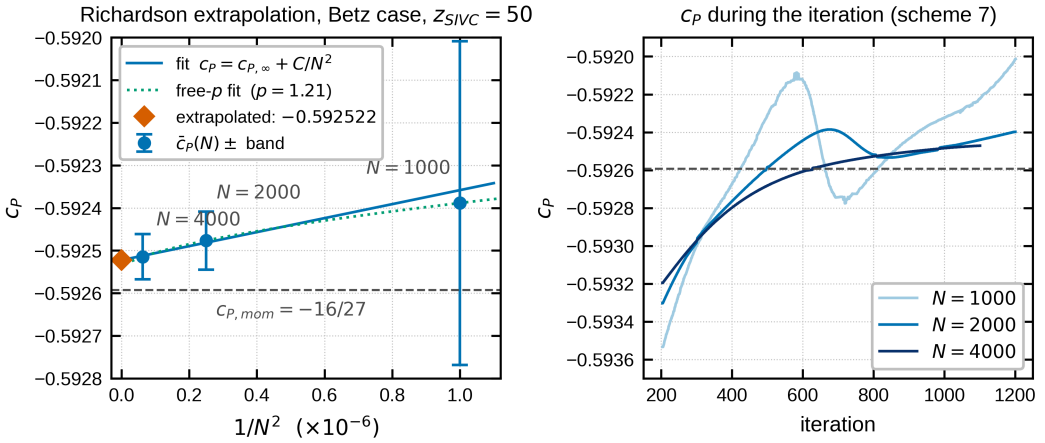


Figure 3. Betz case, $z_{SIVC} = 50$, midpoint collocation, scheme 7. (**Left**) Richardson extrapolation of $c_P(N)$ over $1/N^2$ with the fluctuation bands as error bars; the extrapolated value is -0.592522. (**Right**) Evolution of c_P during the iteration for $N = 1000$, 2000, and 4000; the dashed line is $c_{P,mom} = -16/27$.

3.4. Node Collocation: A Unique Fixed Point

The node-collocation discretization of Section 2.4 changes this picture qualitatively. Table 4 lists the converged results for the Betz case: the residual $\max|\Delta\psi|$ reaches machine level ($\sim 10^{-12}$), there is no c_P band and no drift, i.e., the iteration converges to a *unique* fixed point. The error in c_P saturates between $N = 1600$ and $N = 3200$: the fixed points converge (Aitken limit) to $c_{P,lim} = -0.592545$, leaving an N-independent *model* bias of $+4.7 \times 10^{-5}$ with respect to momentum theory, while the pre-saturation discretization error decays with an observed order $p \approx 1$ (Figure 4). Already at $N = 1600$ the error is $+4.9 \times 10^{-5}$, i.e., better than the midpoint scheme at $N = 4000$.

Table 4. Node collocation with a spacing-proportional kernel (Section 2.4), Betz case: the iteration converges to a unique fixed point—residuals at machine level, no c_P band, no drift.

N	$\max\|\Delta\psi\|$	c_P	$c_P - (-16/27)$
400	4×10^{-12}	-0.5920118	$+5.8 \times 10^{-4}$
800	6×10^{-12}	-0.5923623	$+2.3 \times 10^{-4}$
1600	4×10^{-12}	-0.5925434	$+4.9 \times 10^{-5}$
3200	9×10^{-12}	-0.5925454	$+4.7 \times 10^{-5}$

Separating the origin of the remaining bias—truncation of the vortex tube at $L_{tube} = 30\, R_{wake}$ versus the kernel model at the tube junction and at the edge—requires runs with $N \propto L_{tube}$; at fixed N, enlarging L_{tube} degrades the result because all cells coarsen,

the same resolution/truncation confounding as in the z_{SIVC}-study above. In contrast to midpoint collocation, the remaining c_P error is a smooth, pure discretization error without band or drift, so that Richardson extrapolation is clean (Figure 4). The edge singularity itself remains kernel-smoothed; resolving the conjectured $1/\sqrt{s}$ zone (Section 5) would still require an analytic edge cell or a multivalued sheet parametrization.

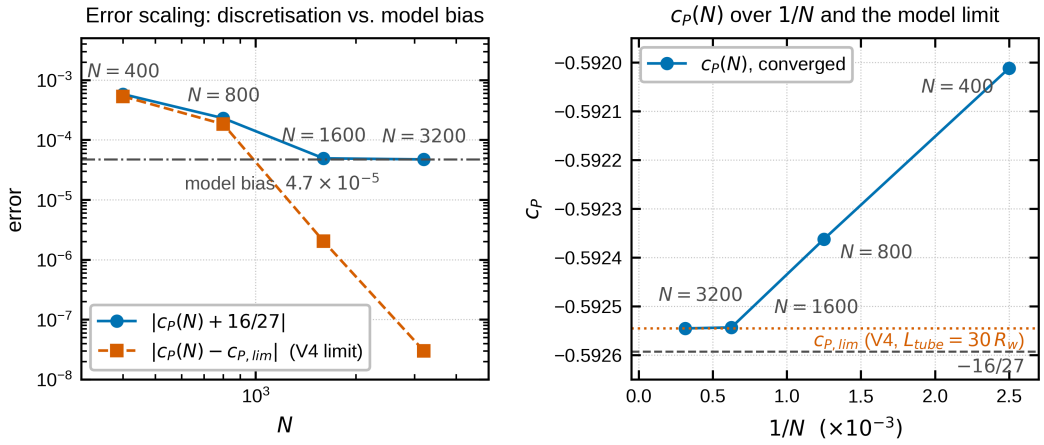


Figure 4. Node collocation, N-study for the Betz case. (**Left**) Error scaling of the converged fixed points: circles, distance to $-16/27$; squares, distance to the model limit $c_{P,lim} = -0.592545$. (**Right**) $c_P(N)$ over $1/N$ together with the model limit and $-16/27$.

4. Results for the Two Reference Cases

4.1. Propeller, $c_T = 1$

The propeller case with $c_T = 1$ is only moderately non-linear: the slipstream contracts to $r_\infty = 0.9239$, i.e., to about 0.93 of the disc radius, and $c_P = 1.207$, to be compared with the linear approximation $c_{P,lin} = 1 + c_T/4 = 1.25$ of [26] (Equation (9.107) therein). Figures 5–7 compare the computed axial velocity and vortex strength along the slipstream, and the streamline pattern, with the data of van Kuik [19]. The agreement is good over the whole range except for the immediate vicinity of the disc edge, $z \lesssim 10^{-3}$, where the two codes deviate—exactly the region discussed in Section 5. The computed edge streamline coincides with $\psi_{wake} = 0.60355339$ from Equation (6), which is an independent check of the converged solution.

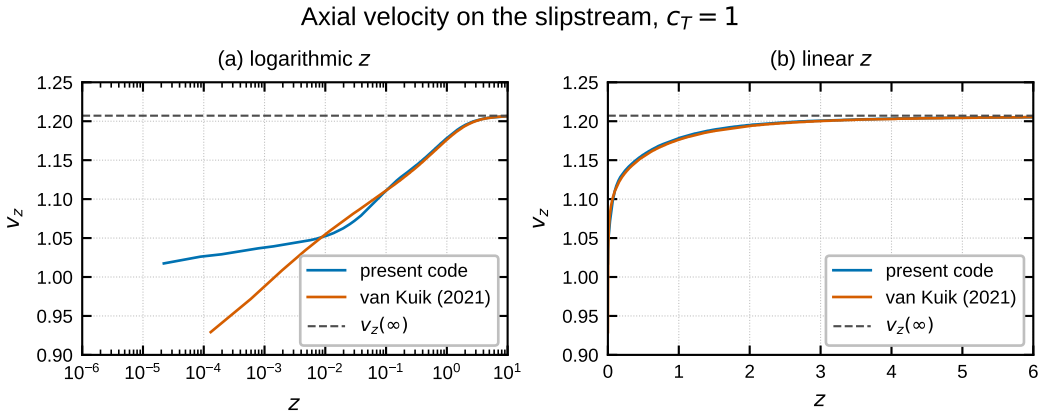


Figure 5. Axial distribution of the axial velocity v_z (inflow included) on the slipstream, $c_T = 1$: present code, data of van Kuik [19] and the asymptotic value $v_z(\infty)$. (**a**) Logarithmic axis, showing the edge region; (**b**) the same data on a linear axis. Curves are shown up to $z = 10$, beyond which both codes append their semi-infinite cylinder.

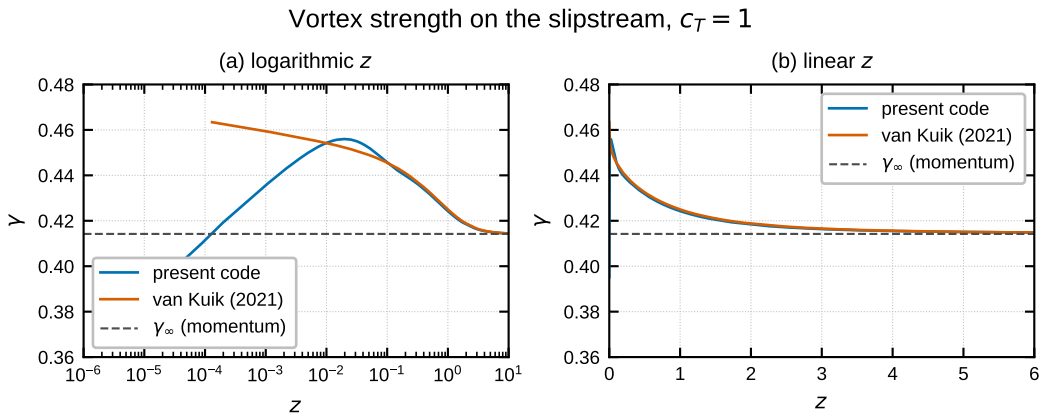


Figure 6. Axial distribution of the vortex strength γ on the slipstream, $c_T = 1$: present code, data of van Kuik [19] and the momentum-theory value γ_∞. (**a**) Logarithmic and (**b**) linear axis. The maximum at $z \approx 2 \times 10^{-2}$ in (**a**) separates the regularized edge region from the wake-development region, see text.

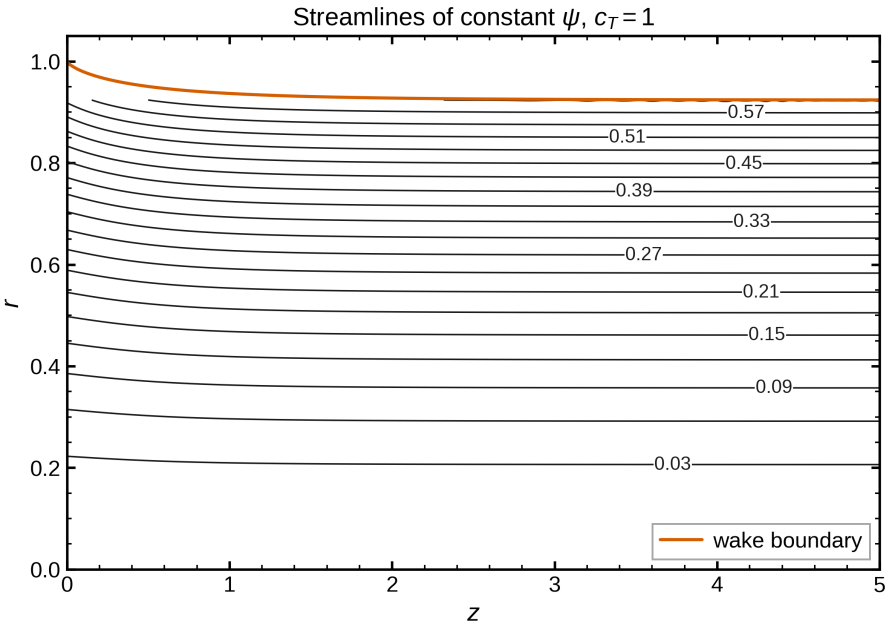


Figure 7. Computed streamlines (lines of $\psi = \text{const.}$) for $c_T = 1$; the wake boundary is drawn in orange. The edge streamline coincides with $\psi_{wake} = 0.60355339$.

The distributions along the slipstream are shown both on logarithmic and on linear axes (panels (a) and (b) of Figures 5, 6 and 8–10). The logarithmic panels are needed to display the edge region, which extends over several decades of z; the linear panels show how close the agreement between the two codes actually is over the part of the wake that determines the loading. The shape of the curves—the S-shape of $v_z(z)$ on logarithmic axes in Figure 5a, and the maximum of γ at $z \approx 2 \times 10^{-2}$ in Figure 6a—reflects two distinct regions. For $z \gtrsim 10^{-2}$ the sheet velocity u_s is governed by the wake development on the scale of the disc radius: u_s is the mean of the velocities on the two sides of the sheet, which inside the wake increases from the disc value towards $1 + \sqrt{1 + c_T}$ and outside relaxes to the free-stream value, so that u_s approaches its asymptote $u_s(\infty) = \frac{1}{2}(1 + \sqrt{1 + c_T}) = 1.207$ on the scale $z \sim 0.1 \ldots 3$. A transition between two plateaus over $z = O(1)$ appears as an inflection on logarithmic axes; on linear axes (panel b), it is the ordinary monotone approach to the asymptote, without any inflection. Since the sheet is force free, $\gamma\, u_s = -c_T/2$, every extremum of u_s is mirrored by an extremum of γ, and γ decreases monotonically towards γ_∞ over the same range. For $z \lesssim 10^{-2}$, in contrast, u_s is dominated by the radial velocity

of the regularized edge singularity, and here the two codes differ: the present code yields a bounded γ that *decreases* towards the edge, whereas van Kuik's data continue to rise (Section 5). The maximum of γ in Figure 6a therefore marks the boundary between the edge region and the wake-development region, not a physical feature of the flow.

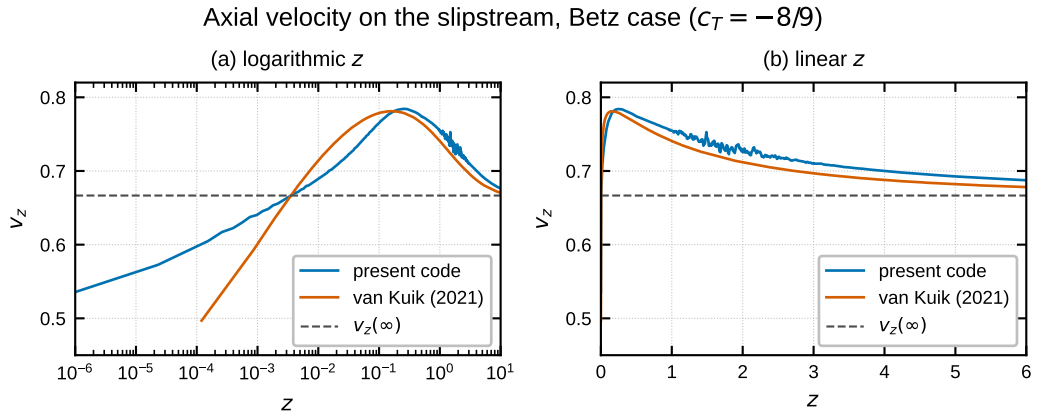


Figure 8. Axial distribution of the axial velocity v_z (inflow included) on the slipstream, Betz case ($c_T = -8/9$): (**a**) logarithmic and (**b**) linear axis. Note the maximum at $z \approx 0.2$, see text.

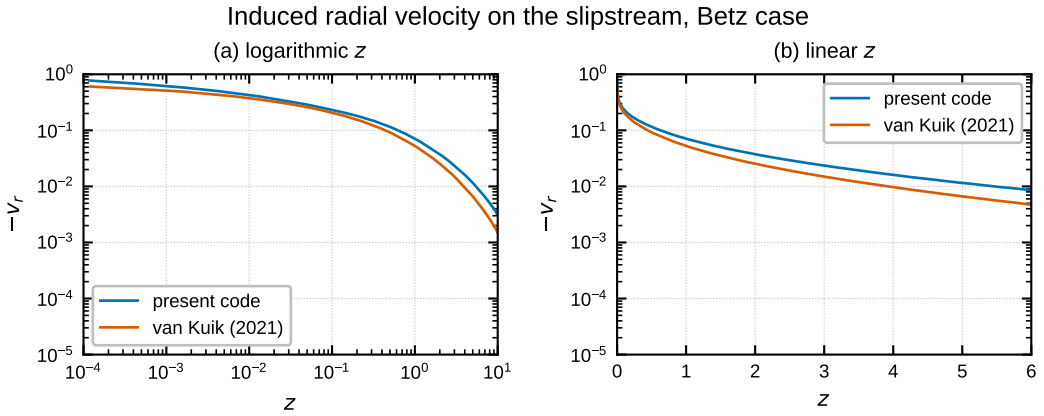


Figure 9. Axial distribution of the induced radial velocity on the slipstream, Betz case: (**a**) logarithmic and (**b**) linear axis (ordinate logarithmic in both panels).

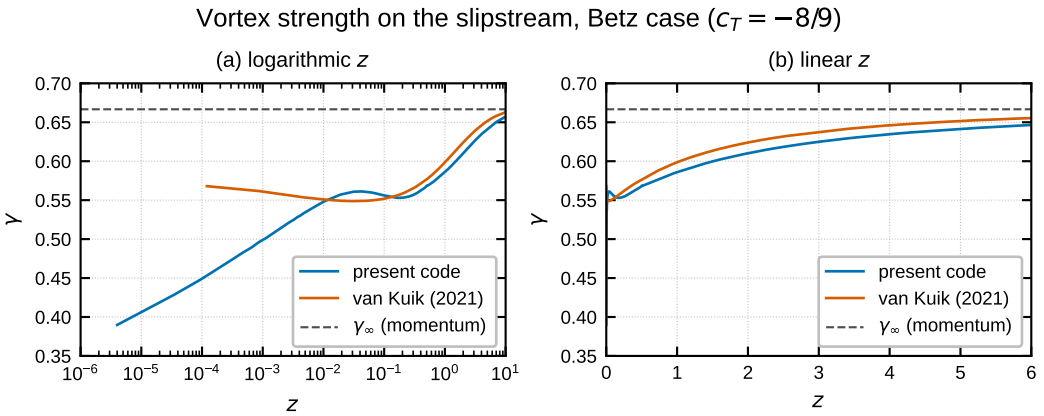


Figure 10. Axial distribution of the vortex strength on the slipstream, Betz case: (**a**) logarithmic and (**b**) linear axis. Note the logarithmic decrease towards the disc edge (small z), which corresponds to the fitted exponent $a \approx 0$ of Table 5, and the minimum at $z \approx 0.2$ that mirrors the maximum of v_z in Figure 8.

Table 5. Fitted edge exponents a of $\gamma \propto s^a$ (Betz case, $z_{SIVC} = 25$, scheme 7, converged solutions).

Fit Window (Rings)	s-Range	a ($N = 600$)	a ($N = 1200$)
2–20	$5 \times 10^{-4} \ldots 4 \times 10^{-2}$	-0.04	$+0.02$
3–40	$8 \times 10^{-4} \ldots 1.5 \times 10^{-1}$	-0.03	-0.02
5–80	$1 \times 10^{-3} \ldots 6 \times 10^{-1}$	$+0.01$	-0.02

4.2. Betz Turbine, $c_T = -8/9$

For the Betz case the slipstream expands to $r_\infty = \sqrt{2}$ and $\psi_{wake} = 1/3$. Figures 8–11 show the axial and radial induced velocities, the vortex strength and the streamline pattern. Both v_z and v_r tend to finite values as $z \to 0^+$ in these regularized solutions—a point taken up in Section 5. The converged power coefficient is $c_P = -0.59251 \pm 0.00007$ (Section 3.3) with midpoint collocation and $c_P = -0.5925454$ with node collocation at $N = 3200$ (Section 3.4), against the momentum-theory value $-16/27 = -0.592593$.

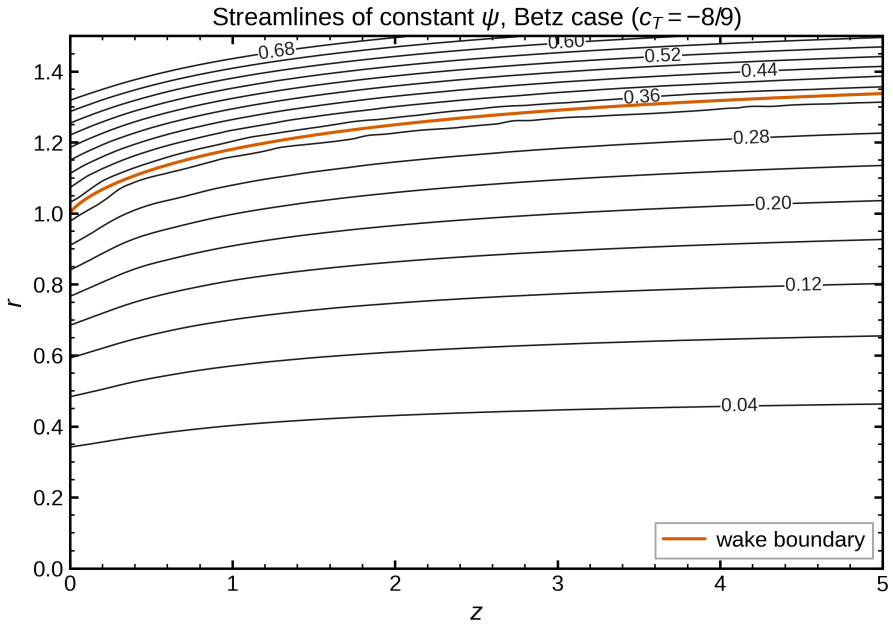


Figure 11. Computed streamlines for the Betz case, $c_T = -8/9$; orange: slipstream, $\psi_{wake} = 0.33333$.

The Betz case shows the same two regions as the propeller case, but with a non-monotone wake development: v_z on the sheet passes through a maximum of ≈0.78 at $z \approx 0.2$ (Figure 8), above its asymptote $\frac{1}{2}(1 + \sqrt{1 + c_T}) = 2/3$, and γ correspondingly through a minimum (Figure 10), again because $\gamma\, u_s$ is constant along the sheet. The overshoot is a displacement effect of the expanding wake: the outer flow is accelerated as it passes around the expanding stream tube and relaxes to the free-stream value only several radii downstream, while the inner velocity decreases from the disc value $2/3$ to the far-wake value $1/3$ on a similar scale, so that their mean—the sheet velocity—first rises and then falls. Both codes reproduce this maximum at the same position and height, which is a useful check because the feature is independent of the treatment of the edge. Below $z \approx 10^{-2}$ the edge region takes over and the codes separate as in the propeller case, the present code with a bounded γ that decreases logarithmically towards the edge (Table 5), van Kuik's with a rising γ. The radial velocity (Figure 9) has no extremum; it is largest at the edge and decays algebraically, the two codes differing by a nearly constant factor for $z \gtrsim 10^{-1}$ that reflects the slightly different converged sheet shapes. The small ripple of the present-code curve for $1 \lesssim z \lesssim 3$, visible on the linear axis of Figure 8b, is the trace of the saw-tooth mode of the midpoint scheme (Section 3.2) in this run; its amplitude

is of the order of 10^{-2} in v_z, it does not affect c_P beyond the band discussed in Section 3.3, and it is removed by the vortex kernel of the node-collocation scheme (Section 2.4).

5. The Disc-Edge Singularity

Along a force-free vortex sheet, $\gamma\, u_s = -c_T/2$ is constant. Van Kuik [5,16] proposes that at the disc edge the wake boundary rolls up into a self-similar (Prandtl/Kaden-type) spiral whose unrolled strength diverges as

$$\gamma(s) \propto s^{-1/2}, \qquad s \to 0, \tag{16}$$

with s the arc length measured from the edge. Is Equation (16) an established result or a hypothesis? A review of the literature together with the numerical evidence of the present model gives the following picture.

5.1. What Is Established

(a) **The linear (frozen-wake) model is singular at the rim.** For a semi-infinite vortex cylinder of *constant* strength, the induced velocity field is singular at the rim: v_z diverges logarithmically and $\partial v_r/\partial s \to \infty$. This is analytic—it is visible in the very Branlard expressions [4] used in this code—and Chattot [17] derives from the Biot–Savart law that the linearized slip line behaves as $r - R \propto -x \ln x$ near the edge.

(b) **The non-linear force-free problem is singular at the leading edge of the sheet.** All potential-flow computations that let γ adjust to the force-free condition find the sheet strength growing (resolution-limited) towards the leading edge. Van Kuik [27] states that "in all flow cases the distributions have a singularity at the leading edge", with a load-dependent strength; see also [12]. The qualitative statement "the disc edge is singular" is therefore established.

5.2. The $1/\sqrt{s}$ Spiral: Strongly Supported, Not Proven

The analytical basis of Equation (16) is the local non-linear analysis of Schmidt and Sparenberg [28] for a large constant normal load. Van Kuik revisited the edge in [16] and constructed the flow induced by, and a steady solution for, Prandtl's self-similar vortex-sheet spirals [29,30]. Equation (16) is exactly the Kaden roll-up law, which is rigorously established for the *unsteady* two-dimensional similarity problem (see, e.g., [20]). Independent support comes from Spalart [31], who concludes—explicitly labeling it a conjecture—that "the cross-section of the vortex sheet probably begins with a 45° spiral", supported by a viscous numerical solution. In contrast, Chattot [17] obtains, from a linearized analysis with a *prescribed constant* sheet strength, logarithmic velocity singularities, and a bounded γ; the disagreement is traceable to that assumption, since it is precisely the force-free coupling $\gamma = -c_T/(2u_s)$ that drives $\gamma \to \infty$ where $u_s \to 0$. No free-wake computation has resolved the spiral, and no experiment resolves the exponent. Thus, the *existence* of the singularity is established, whereas the *specific form* (16) is a well-founded, independently supported, but unproven hypothesis.

5.3. Numerical Evidence from the Present Model

The converged solutions of the present model show a *bounded* edge strength. A log–log fit $\gamma \propto s^a$ over the first rings of converged double-precision solutions (scheme 7) gives the exponents of Table 5: $a = 0.00 \pm 0.04$ over two decades in s, with $\gamma_{edge} \approx 0.55 < \gamma_\infty = 2/3$ and, at matched s, N-independent values. This is consistent with the logarithmic decrease seen in Figure 10.

This result does *not* contradict the spiral picture. A discretization of the present class is structurally unable to represent it, for three independent reasons:

1. the single-valued parametrization $r_{sl}(z)$ of the sheet excludes any multivalued (rolled-up) geometry;
2. the self-induction term, Equations (7) and (8) (or the vortex kernel of Section 2.4), regularizes the Biot–Savart kernel at the panel scale ds;
3. the force-free update evaluated with this regularized velocity keeps γ bounded, because u_s cannot reach zero.

The code therefore converges to the regularized solution of the *no-roll-up* problem, which is why the present findings differ from van Kuik's $s^{-1/2}$ *and* from Chattot's constant-γ picture. Practically, the singularity is integrable ($\int \gamma\, ds < \infty$), so c_P converges unaffected; its footprint in the computation is the saturation of $\max|\Delta\psi|$ at the first ring(s) and the c_P band of Section 3.3. Any attempt to settle the exponent numerically will require either an analytic edge element or a multivalued sheet parametrization—neither of which is contained in any of the free-wake AD codes known to the author.

5.4. A Note on the "Fine-Tuning" of van Kuik and Lignarolo

The convergence scheme of [12] (Appendix B.3 therein) switches, after convergence of the ψ-condition with damping 0.05, to the condition $v_n = 0$, applied as $\Delta r_i = -v_{n,i}\, d$ with $d = 0.0025$ ("fine tuning"). Transferring this second phase to a midpoint-collocation code fails structurally: after ψ-convergence, v_n at the first ≈5 rings is $O(1)$—0.9 at the first ring—which is a discretization artifact of midpoint collocation and not a usable residual; stepping on it destroys the solution for either sign of the update. In the node-collocation discretization of Section 2.4 the artifact disappears ($v_n \approx 3 \times 10^{-2}$ at the edge), but the v_n-phase is then unnecessary, because the ψ-iteration already converges to machine accuracy. It is worth noting that even in [12] the fine-tuning does not resolve the edge: a 40% violation of $\Delta p_{sheet} = 0$ is reported at the first ring, and the authors conclude that the boundary conditions hold for a vortex sheet but not for its leading edge.

6. Discussion

Six model and discretization parameters were found to influence the accuracy of the computed solution: (i) the number of rings N; (ii) the axial location z_{SIVC} of the semi-infinite cylinder; (iii) the number of integration points at the disc; (iv) the model used for the self-induction; (v) the initial and converged shape of the slipstream; and (vi) the number and distribution of vortex rings close to the disc edge. This confirms van Kuik's finding [5] that these parameters are interrelated rather than independent. Nevertheless, increasing N always increases the accuracy, whereas increasing z_{SIVC} at fixed N does not (Section 3.3).

The results suggest the following practical recommendations for free-wake actuator-disc computations:

1. **Do not stop the iteration on the momentum-theory deviation.** Use the sheet residual, monitor the unweighted $\max|\Delta\psi|$ in addition to the ds-weighted mean, and treat errc_P as a *verification* quantity, never as a convergence criterion.
2. **Quote c_P as "average ± band"** when using midpoint collocation, and reduce the band by an N-study with Richardson extrapolation rather than by more iterations.
3. **Use $z_{SIVC} \approx 50$** and invest the remaining computational effort in N.
4. **Prefer node collocation with a spacing-proportional kernel** if a unique fixed point is required, e.g., for gradient-based optimization or for embedding the model in a larger solver. A kernel radius proportional to the local spacing is essential on clustered grids.
5. **Do not expect the edge exponent from this class of model.** A bounded γ at the edge is a property of the regularization, not a physical result.

Returning to Equation (13): for the sheet residual, the improved iteration demonstrably satisfies the requirement, and node collocation does so with machine-level residuals. For errc_P the requirement can hold only in the combined limit (iterations $\to \infty$, $N \to \infty$, $z_{SIVC} \to \infty$), because at fixed discretization errc_P has a floor that no iteration can undercut. This distinction is elementary, but it is not usually made explicit in the actuator-disc literature, where agreement with momentum theory to a given number of digits is often presented as evidence of numerical convergence.

The limitations of the present work should be stated clearly. The model is restricted to a uniformly loaded, axisymmetric, steady, inviscid disc without swirl; the generalization to non-uniform loading exists analytically [15] but has not been implemented here. The steady solution is an idealization: the real wake is unstable and rolls up into discrete vortex clumps a few radii downstream (Section 3.2), so the converged sheet describes the time-averaged wake that underlies momentum theory, not the instantaneous flow. Statements about "convergence" in this paper are statements about the discrete model equations, not about the physical stability of the wake. The remaining model bias of the node-collocation scheme (4.7×10^{-5} in c_P) has not been decomposed into its tube-truncation and kernel contributions, which would require runs with $N \propto L_{tube}$. Finally, neither discretization resolves the edge region itself, so the results of Section 5 bound what such models can say about the singularity rather than settling the question.

7. Conclusions

An independent, open-source FORTRAN 90/95 implementation of the vortex-ring/vortex-cylinder model for a uniformly loaded actuator disc, together with a 1:1 Python replica, was used to examine the numerical behavior of this model class for the propeller case $c_T = 1$ and the Betz case $c_T = -8/9$. The conclusions are:

1. The sheet residual errsl and the momentum-theory deviation errc_P measure different things. errsl can be driven below 10^{-8} while errc_P stagnates at a discretization floor; errc_P is not monotone and is therefore unsuitable as a stopping criterion.
2. A damping factor $\propto \sqrt{z}$ (optionally with Anderson acceleration) stabilizes the Kelvin–Helmholtz saw-tooth mode and reaches the residual floor within a few hundred iterations, where the previously used damping $\propto z$ required 10^4 iterations or never settled.
3. With midpoint collocation, c_P retains a fluctuation band ($\pm 4 \times 10^{-4}$ at $N = 600$, $z_{SIVC} = 25$) that reflects the under-determined edge region. An N-study with Richardson extrapolation gives $c_P = -0.59251 \pm 0.00007$ for the Betz case, i.e., within 10^{-4} of $-16/27$.
4. Node collocation with a spacing-proportional vortex kernel and a pinned first ring converges with uniform damping to a unique fixed point (residuals $\sim 10^{-12}$, no band, no drift) and reaches $c_P - (-16/27) = +4.7 \times 10^{-5}$, a residual *model* bias that is independent of N.
5. The converged solutions exhibit a bounded edge strength with fitted exponent $a = 0.00 \pm 0.04$, differing from both the $\gamma \propto s^{-1/2}$ spiral and the constant-γ picture. This is the expected behavior of a single-valued, regularized sheet discretization and does not decide between the two proposals; the existence of the edge singularity is established, its specific form remains an open question.

Future work should address the decomposition of the remaining model bias, the extension to non-uniformly loaded discs, and—for the edge question—an analytic or multivalued edge element capable of representing a rolled-up sheet.

Funding: This research received no external funding.

Institutional Review Board Statement: Not applicable.

Informed Consent Statement: Not applicable.

Data Availability Statement: The FORTRAN source code, its Python replica, the configuration files of all cases discussed in this paper and the post-processing scripts are openly available at https://github.com/Schaffarczyk/RingsCylinderActuatorDisk/ (accessed on 10 September 2026). The reference data of [19] are available from their author.

Acknowledgments: The author would like to thank Gijs van Kuik for providing his reference data ($c_T = 1$ and $c_T = -8/9$) and Emmanuel Branlard for helpful discussions.

Conflicts of Interest: The author declares no conflicts of interest.

Abbreviations

AD	actuator disc
EWMA	exponentially weighted moving average
KH	Kelvin–Helmholtz
SIVC	semi-infinite vortex cylinder

References

1. van Kuik, G.; Sørensen, J.; Okulov, V. Rotor theories by Professor Joukowsky: Momentum theories. *Prog. Aerosp. Sci.* **2015**, *73*, 1–18. [CrossRef]
2. Schaffarczyk, A. *Introduction to Wind Turbine Aerodynamics*, 3rd ed.; Springer: Berlin/Heidelberg, Germany, 2024.
3. Sørensen, J. *General Momentum Theory for Horizontal Axis Wind Turbines*; Springer International Publishing: Cham, Switzerland, 2016.
4. Branlard, E. *Wind Turbine Aerodynamics and Vorticity-Based Methods*; Springer: Cham, Switzerland, 2017.
5. van Kuik, G. *The Fluid Dynamic Basis for Actuator Disc and Rotor Theories*, 2nd ed.; IOS Press: Amsterdam, The Netherlands, 2022.
6. Johnson, W. *Helicopter Theory*; Princeton University Press: Princeton, NJ, USA, 1980. Reprinted in Dover Publications: New York, NY, USA, 1994.
7. Leishman, J. *Principles of Helicopter Aerodynamics*, 2nd ed.; Cambridge University Press: Cambridge, UK, 2006.
8. Bhagwat, M.; Leishman, J. Stability, consistency and convergence of time-marching free-vortex rotor wake algorithms. *J. Am. Helicopter Soc.* **2001**, *46*, 59–71. [CrossRef]
9. Winckelmans, G.; Leonard, A. Contributions to vortex particle methods for the computation of three-dimensional incompressible unsteady flows. *J. Comput. Phys.* **1993**, *109*, 247–273. [CrossRef]
10. Miller, R. Vortex theory for hovering rotors. *AIAA J.* **1982**, *20*, 1754–1756. [CrossRef] [PubMed]
11. Øye, S. A simple vortex model. In *Proceedings of the 3rd IEA Symposium on the Aerodynamics of Wind Turbines (IEA Annex XI)*; Harwell, ETSU: Oxfordshire, UK, 1990.
12. van Kuik, G.; Lignarolo, L. Potential flow solutions for energy extracting actuator disc flows. *Wind Energy* **2016**, *19*, 1391–1406. [CrossRef]
13. Bontempo, R.; Manna, M. A ring-vortex free-wake model for uniformly loaded propellers. Part I—Model description. In Proceedings of the 73rd Conference of the Italian Thermal Machines Engineering Association (ATI 2018), Pisa, Italy, 12–14 September 2018; Volume 148.
14. Bontempo, R.; Manna, M. A ring-vortex free-wake model for uniformly loaded propellers. Part II—Solution procedure and analysis of the results. In Proceedings of the 73rd Conference of the Italian Thermal Machines Engineering Association (ATI 2018), Pisa, Italy, 12–14 September 2018; Volume 148.
15. Conway, J. Exact actuator disk solutions for non-uniform heavy loading and slipstream contraction. *J. Fluid Mech.* **1998**, *365*, 235–267. [CrossRef]
16. van Kuik, G. The edge singularity of an actuator disc with a constant normal load. In Proceedings of the 22nd ASME Wind Energy Symposium, Reno, NV, USA, 6–9 January 2003. [CrossRef]
17. Chattot, J.J. On the edge singularity of the actuator disk model. *J. Sol. Energy Eng.* **2021**, *143*, 014502. [CrossRef]
18. Chapman, S. *Fortran 90/95 for Scientists and Engineers*, 2nd ed.; McGraw-Hill: New Delhi, India, 2013.
19. van Kuik, G. (Delft University of Technology, Delft, The Netherlands). Reference data for the uniformly loaded actuator disc, $c_T = 1$ and $c_T = -8/9$. Personal communication, 2021.

20. Saffman, P. *Vortex Dynamics*; Cambridge University Press: Cambridge, UK, 1992.
21. Carlson, B.; Notis, E. Algorithm 577: Algorithms for incomplete elliptic integrals. *ACM Trans. Math. Softw.* **1981**, *7*, 398–403. [CrossRef]
22. The GCC Team. The GNU Fortran Compiler. Available online: https://gcc.gnu.org/fortran/ (accessed on 27 July 2026).
23. Widnall, S. The stability of a helical vortex filament. *J. Fluid Mech.* **1972**, *54*, 641–663. [CrossRef]
24. Sørensen, J. Instability of helical tip vortices in rotor wakes. *J. Fluid Mech.* **2011**, *682*, 5–53. [CrossRef]
25. Lignarolo, L.; Ragni, D.; Krishnaswami, C.; Chen, Q.; Simão Ferreira, C.; van Bussel, G. Experimental analysis of the wake of a horizontal-axis wind-turbine model. *Renew. Energy* **2014**, *70*, 31–46. [CrossRef]
26. Breslin, J.; Andersen, P. *Hydrodynamics of Ship Propellers*; Cambridge University Press: Cambridge, UK, 1994.
27. van Kuik, G. On the velocity at wind turbine and propeller actuator discs. *Wind Energy Sci.* **2020**, *5*, 855–865. [CrossRef]
28. Schmidt, G.; Sparenberg, J. On the edge singularity of an actuator disk with large constant normal load. *J. Ship Res.* **1977**, *21*, 125–131. [CrossRef]
29. van Kuik, G. The flow induced by Prandtl's self-similar vortex sheet spirals at infinite distance from the spiral kernel. *Eur. J. Mech. B/Fluids* **2004**, *23*, 607–616. [CrossRef]
30. van Kuik, G. A steady solution for Prandtl's self-similar vortex sheet spirals. *Eur. J. Mech. B/Fluids* **2009**, *28*, 296–298. [CrossRef]
31. Spalart, P. On the simple actuator disk. *J. Fluid Mech.* **2003**, *494*, 399–405. [CrossRef]

Disclaimer/Publisher's Note: The statements, opinions and data contained in all publications are solely those of the individual author(s) and contributor(s) and not of MDPI and/or the editor(s). MDPI and/or the editor(s) disclaim responsibility for any injury to people or property resulting from any ideas, methods, instructions or products referred to in the content.